Velocity Estimation of Fast Moving Targets using a Single SAR Sensor

PAULO A. C. MARQUES, Member, IEEE
Instituto Superior de Engenharia de Lisboa
Portugal

JOSÉ M. B. DIAS, Member, IEEE
Instituto Superior Técnico
Portugal

A new methodology is presented to retrieve slant-range velocity estimates of moving targets inducing Doppler-shifts beyond the Nyquist limit determined by the pulse repetition frequency (PRF). The proposed approach exploits the linear dependence (not subject to PRF limitations) of the Doppler-shift with respect to the slant-range velocity, at each wavelength. Basically, we propose an algorithm to compute the skew of the two-dimensional spectral signature of a moving target. Distinctive features of this algorithm are its ability to cope with strong range migration and its efficiency from the computational point of view. By combining the developed scheme to retrieve the slant-range velocity with a methodology proposed earlier to estimate the velocity vector magnitude, the full velocity vector is unambiguously retrieved without increasing the mission PRF. The method gives effective results even when the returned echoes of the moving targets and the static ground overlap completely, provided that the moving targets signatures are digitally spotlighted and the signal-to-clutter ratio (SCR) is, roughly, greater than 14 dB. The effectiveness of the method is illustrated with simulated and real data. As an example, slant-range velocities of moving objects with velocities between 6 and 12 times the Nyquist velocity are estimated with accuracy better than 3%.

Manuscript received October 16, 2002; revised December 2, 2003; released for publication November 1, 2004.

IEEE Log No. T-AES/41/1/842440.

Refereeing of this contribution was handled by P. Lombardo.

This work was supported by the Fundação para a Ciência e Tecnologia, under the project POSI/34071/CPS/2000.

Authors' addresses: P. A. C. Marques, Instituto Superior de Engenharia de Lisboa, Dept. Engenharia da Electronica e das Comunicacoes, Ed. 5, Sala 16, R. Conselheiro Emidio Navarro, 1, Lisboa 1949-014, Portugal, E-mail: (pmarques@isel.pt); J. M. B. Dias, Instituto de Telecomunicações, IST, Av. Rovisco Pais, 1049-001 Lisboa, Portugal.

I. INTRODUCTION

A moving target induces in the synthetic aperture radar (SAR) returned signal a Doppler-shift and a Doppler-spread in the slow-time[1] frequency domain [2]. Most techniques proposed in the recent literature to image moving targets and estimate their velocity parameters take advantage of this knowledge, e.g. [3], [4], [5], and [6]. Assuming a broadside geometry, the cross-range and slant-range velocities of a moving target are responsible for the spread and for the Doppler-shift, respectively, both in the slow-time frequency domain. Given a pulse repetition frequency (PRF), the Doppler-shift $f_D = 2v_x/\lambda$, where v_x is the target slant-range velocity and λ is the signal wavelength, is confined to

$$\frac{-\text{PRF}}{2} < f_D \leq \frac{\text{PRF}}{2}. \tag{1}$$

If the received signal is aliased (i.e., the induced Doppler-shift exceeds PRF/2) it has been mostly accepted that the true moving target slant-range velocity cannot be uniquely determined using a single antenna and a single pulse scheduling [7, 8]. Classical solutions to process such targets with a single antenna consist in increasing the PRF [7] or, alternatively, in using a nonuniform PRF as proposed in [8] and [9]. Increasing the PRF shortens the unambiguous range swath and increases the memory requirements to store the received signal. The use of a nonuniform PRF requires a nonconventional pulse scheduling, introducing complexity in image reconstruction algorithms.

In [10], a method has been proposed which copes with target motion induced Doppler-shifts up to (3/2) PRF. This is done by evaluating the Doppler-shift—possibly affected by aliasing—together with the range walk of the target. The present article, which elaborates on ideas presented in [11], proposes a novel technique to estimate the slant-range velocity of ground-based moving targets with velocities above the Nyquist limit. The method takes advantage of the linear dependence of the Doppler-shift on the slant-range velocity, at each fast-time frequency. In the two-dimensional frequency domain, a moving target echo exhibits a skew not subject to PRF limitations. In [12] this fact has already been exploited to retrieve the spectral support of SAR signals, with application to low contrast ground scenes in spaceborne SAR. In these scenarios the ground behaves as a moving target due to the Earth rotation relatively to the radar platform. The method proposed therein works by

[1] Herein, we follow Soumekh's terminology (see [1, ch. 2]) according to which the cross-range coordinates and the round-trip time are termed slow-time domain and fast-time domain, respectively. This terminology stems from the fact that the motion of the radar platform is much slower than the speed of light at which the transmitted and backscattered pulses propagate.

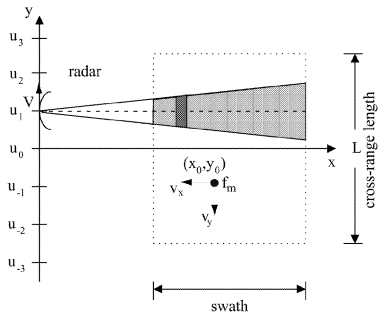

Fig. 1. Slant-plane of SAR broadside geometry.

applying a linear regression on the estimated Doppler centroids at each fast-time frequency. The problem that we are dealing with here cannot be solved by the same technique, because we are interested in returns from approximately point-like moving targets (e.g., many man-made objects), relatively to the ground. Even after digitally spotlighting the moving target signatures [13], i.e., cropping small areas of focused or roughly focused scenes, the ground echoes exhibit sufficient power to corrupt the estimates given by spectral centroid type estimators. We present a technique here able to cope with this scenario. For scenes with signal-to-clutter ratio[2] (SCR) higher than 14 dB, the proposed estimator is effective, even when the ground echoes are completely superimposed, in the frequency domain, on the moving objects echoes.

This paper is organized as follows. In Section II we review basic properties of moving target echoes in SAR and present the proposed methodology to retrieve unaliased estimates of the slant-range velocity. In Section III we show results taking real and simulated data to illustrate the effectiveness of the proposed scheme. In the appendix we derive expressions supporting the main text and compute theoretical bounds.

II. PROPOSED APPROACH

This section derives the properties of the SAR raw data echoed from a moving target in the two-dimensional frequency domain. After addressing the properties of the clutter raw data in the two-dimensional frequency domain, we propose a methodology to unambiguously estimate the slant-range velocities of multiple moving targets.

Let us consider the SAR scenario illustrated in Fig. 1, where the radar travels at constant velocity V and constant altitude along the flight path (cross-range direction). The antenna transmits microwave pulses and records the backscattered echoes. The illuminated scene contains a moving target with reflectivity f_m, slant-plane coordinates (x_0, y_0) when the SAR platform is at position $y = u_0$, and velocity vector $(-v_x, -v_y)$.[3] Let $p(t)$ be the transmitted pulse when the antenna is at cross-range coordinate u and $S_m(u,t)$ the corresponding received signal. The 2D Fourier transform of the received signal, $S_m(k_u,k)$, where $k_u = 2\pi/\lambda_u$ is the slow-time frequency domain[4] and $k \equiv 2\pi/\lambda$ is the fast-time frequency domain is, after pulse compression, given by [3, 14]

$$S_m(k_u,k) = |P(\omega)|^2 A(k_u,k) f_m e^{-j\sqrt{4k^2-(k_u/\alpha)^2}X} e^{-j(k_u/\alpha)Y} \tag{2}$$

where $P(\omega)$ is the Fourier transform of the transmitted pulse $p(t)$ and $\omega = 2\pi c/\lambda$. Symbols λ and λ_u denote the signal wavelength in the fast-time and in the slow-time frequency domain, respectively, and c is the speed of light. Function $A(k_u,k)$ is the two-way antenna radiation pattern. Symbol $\alpha \equiv \sqrt{\mu^2+\nu^2}$ is the relative speed of the moving target with respect to the radar, where $\nu \equiv (1 + v_y/V)$ and $\mu \equiv v_x/V$ denote, respectively, the moving target relative cross-range and slant-range velocities, with respect to the sensor velocity. The couple (X,Y) are the so-called motion transformed coordinates of the moving target [1, ch. 6.7], [14] and are a rotated and scaled version of coordinates (x_0, y_0), i.e.,

$$\begin{bmatrix} x_0 \\ y_0 \end{bmatrix} = \frac{1}{\alpha} \begin{bmatrix} \nu & -\mu \\ \mu & \nu \end{bmatrix} \begin{bmatrix} X \\ Y \end{bmatrix}.$$

In [14], we have shown that the amplitude modulation term $A(k_u,k)$ of the returned echo from a moving target takes, in the two-dimensional frequency domain, the shape of the two-way antenna radiation pattern according to

$$A(k_u,k) \propto g^2\left(\frac{1}{2\nu}(k_u - 2k\mu)\right) \tag{3}$$

valid for $v_y > -V$, where g is related with the 2D Fourier transform of the electric field at the antenna aperture (see [14] for details).

Relative to a static target, and for a constant wavenumber k, the shape g becomes dilated by 2ν and shifted by $2k\mu$. If the transmitted pulse has bandwidth B, then k is confined to

$$k_{\min} \cong -\frac{\pi B}{c} + k_0 < k \le k_0 + \frac{\pi B}{c} \cong k_{\max} \tag{4}$$

where $k_0 \equiv 2\pi/\lambda_0$ and λ_0 is the carrier wavelength. For a moving target with relative slant-range velocity μ, we see from (3) that the support of the returned signal $S_m(k_u,k)$ exhibits a slope of 2μ with respect to the k axis, as illustrated in Fig. 2. In this figure, $k_{u_{\text{end}}}$ and $k_{u_{\text{start}}}$ denote the Doppler-shifts at the fast-time

[2]The definition of SCR herein used corresponds to the ratio between the peak (squared magnitude) of the correctly focused moving target signal and the covariance of the clutter background.

[3]Since we use notation and results from [13] and [14], we directed velocities v_x and v_y opposite to x and y, in conformity.

[4]In classical SAR jargon, k_u is termed the Doppler domain.

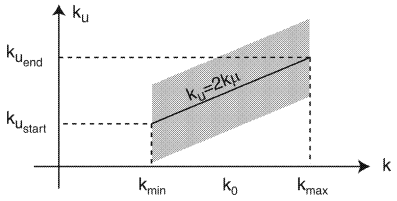

Fig. 2. Support of returned signal from moving target with relative range velocity μ.

frequencies $k_{\max}$ and $k_{\min}$, respectively. We conclude then that

$$\mu = \frac{k_{u_{\text{end}}} - k_{u_{\text{start}}}}{2(k_{\max} - k_{\min})} \tag{5}$$

regardless of the PRF. In the absence of electronic noise and ground clutter, $k_{u_{\text{end}}}$ and $k_{u_{\text{start}}}$ could be inferred using a simple centroid technique. This solution cannot, however, be applied in the case of ground moving targets, because the returned signal coexists with clutter returns in the 2D spectrum. The weight of the clutter can be reduced by spotlighting the moving target area [13]. This process consists in focusing with approximated moving target parameters (recall that the true moving target parameters are not known) and cropping the region containing the target of interest. In the work presented here we focus the target region using static ground parameters ($\alpha = 1$). The moving targets will appear defocused, as their relative velocity α is different from the value used to focus the target region. They span, however, a region that is usually much smaller than the total illuminated scene. Each moving target can thus be reasonably separated from the signatures of the other (moving and stationary) targets. Once the moving target signature is spotlighted in the spatial domain, it is resynthesized back to the 2D frequency domain for further processing.

We show in Appendix A that if the number of the ground scatterers is large, none is predominant, and they are uniformly distributed within a wavelength, then the correlation of the static ground returns, in the (k_u,k) domain, decays very quickly in both dimensions. Concerning moving targets, the same is not true, as shown in the next subsection. Thus, the signals echoed by moving targets have statistical properties quite different from those of the clutter. We exploit these distinct properties here to derive a methodology to unambiguously estimate the moving targets slant-range velocities.

A. Moving Target Signature Properties

The autocorrelation function $R_{SS}(\Delta k_u,k_1,k_2)$ between $S_m(k_u,k_1)$ and $S_m(k_u,k_2)$ with respect to k_u is

$$R_{SS}(\Delta k_u,k_1,k_2) = \int_{-\infty}^{+\infty} S_m(k_u,k_1) S_m^*(k_u - \Delta k_u,k_2) dk_u. \tag{6}$$

From (3) we can write $A(k_u,k_1 + \Delta k) = A(k_u - 2\Delta k\mu,k_1)$. Using this fact and after applying some algebra to (6), we are lead to

$$\begin{aligned} R_{SS}&(\Delta k_u,k_1,k_1 + \Delta k) \\ &\approx |P(\omega_1)|^2 |P(\omega_2)|^2 |f_m|^2 e^{-j[(\Delta k_u/\alpha)Y - (2\Delta k - (\Delta k_u^2/4(k_1+\Delta k)\alpha^2))X]} \\ &\quad \times \int_{-\infty}^{+\infty} A(k_u,k_1) A^*(k_u - 2\Delta k\mu - \Delta k_u,k_1) e^{j\phi} dk_u \end{aligned} \tag{7}$$

where $\omega_1 = k_1 c$, $\omega_2 = k_2 c$, $\Delta k = k_2 - k_1$, and

$$\phi = \frac{2k_u \Delta k_u}{4(k_1 + \Delta k)\alpha^2} X. \tag{8}$$

If phase ϕ has an excursion smaller than π in the Doppler interval equivalent to the antenna bandwidth,[5] the last line of (7) is a correlation between $A(k_u,k_1)$ and $A(k_u - 2\Delta k\mu,k_1)$, with respect to k_u, computed at Δk_u. The correlation magnitude $|R_{SS}(\Delta k_u,k_1,k_1 + \Delta k)|$ exhibits a maximum that is linearly dependent on Δk by a factor of 2μ.

The maximum relative slant-range velocity that can be estimated using this methodology is thus imposed by the above referred restriction on phase ϕ. To compute an expression for the maximum relative slant-range velocity that can be estimated, let us consider that the maximum magnitude of the correlation R_{SS} occurs at $\Delta k_u = 2\Delta k\mu$ and that the two-way antenna bandwidth is B_u [rad/m]. Considering that the relative velocity is $\alpha \approx 1$, then the relative slant-range velocity that can be estimated is bounded by

$$|\mu| < \frac{(k + \Delta k)\pi}{B_u \Delta k X}. \tag{9}$$

Bound (9) can be made larger by compensating in (2) the dependency on X using the target area approximate slant-range coordinates; i.e., multiplying signal $S_m(k_u,k)$ in (2) by $\exp\{j\sqrt{4k^2 - (k_u/\alpha')^2}X'\}$, where X' is the target approximate slant-range coordinate in the unfocused image and $\alpha' = 1$ is the target approximate velocity vector magnitude. In this way, phase ϕ, although not completely compensated, will exhibit a smaller excursion.

As a numerical example of bound (9), let us consider the AER-II SAR system parameters mentioned in [15] and an error of 50 m in the slant-range coordinate X of the moving target. Assuming the Transall aircraft cruise speed of 495 km/h, the maximum unambiguous velocity is approximately 200 km/h, which is sufficient for most man-made ground vehicles.

Another possibility to make the limit (9) less tight consists in partitioning the overall pulse-bandwidth into smaller bands, and computing μ by averaging the estimates of all bands.

[5]Herein we use the term antenna bandwidth to designate the slow-time wavenumber interval corresponding to the −3 dB two-way beamwidth of the antenna.

In deriving (7) we have assumed that the antenna pattern $A(k_u,k)$ does not depend on the wavenumber k in the pulse bandwidth interval. This is valid for planar antennas [1, ch. 6.3]. In the case of a curved radar aperture the antenna pattern depends on k. Nevertheless, this dependency does not invalidate the concepts just presented as its effect does not occur in the Doppler domain.

B. Proposed Methodology

In a realistic SAR scenario the received moving target echoes are contaminated with returns from the clutter and with electronic noise. Thus, the received signal $S(k_u,k)$ can be written, in the Fourier domain, as

$$S(k_u,k) = S_m(k_u,k) + S_0(k_u,k) \tag{10}$$

where S_0 is the term due to the clutter plus the electronic noise.

Based on the statistics of S_0 and on expression (2) of S_m, we could derive a maximum likelihood estimator of μ. However, the signal S_m depends on the unknown terms X,Y,α, and $A(k_u,k)$, besides the parameter μ in which we are interested. This dependency introduces complexity in the maximum likelihood approach. By exploiting the structure of the correlation between $S_m(k_u,k_1)$ and $S_m(k_u,k_2)$, we herein adopt a suboptimal solution that is simpler and, nevertheless, effective.

Based on the analysis made in the previous subsection, we present the following methodology to unambiguously compute μ.

1) Estimate a rough location of the moving targets using one of the strategies proposed in recent bibliography (see, e.g., [1], [5], or [16]). Here we adopt a methodology similar to that proposed by Freeman in [5] because it is simple and leads to good results. The strategy consists in first applying a high-pass filter in the (k_u,k) domain with stop-band adjusted to filter out static targets and then performing imaging using static ground parameters. A rough slant-range coordinate X' for each moving target is inferred from its slant-range position.

2) Process the SAR raw data as if there were only static targets. The ground appears focused and the moving targets appear smeared, defocused, and misplaced.

3) For each detected moving target:

a) Digitally spotlight the moving target image in the spatial domain and resynthesize its signature back to the (k_u,k) domain as described in [1, ch. 6.7], obtaining the signal $\hat{S}_m(k_u,k) = S_m(k_u,k) + S_{0R}(k_u,k)$, where S_{0R} denotes the remaining noise after the digital spotlight operation.

b) Compensate phase ϕ using the target approximate slant-range coordinate X' estimated in step 1) and the approximate relative velocity $\alpha' = 1$. This is accomplished by multiplying $\hat{S}_m(k_u,k)$ by $\exp\{j\sqrt{4k^2-(k_u/\alpha')^2}X'\}$. If a more accurate phase compensation is needed, α can be estimated using the algorithm presented in [13].

c) Compute the correlation $R_{\hat{S}\hat{S}}$ between $\hat{S}_m(k_u,k_0)$ and $\hat{S}_m(k_u,k)$ for a set of discrete wavenumbers within the transmitted pulse bandwidth. We obtain then

$$\begin{aligned} R_{\hat{S}\hat{S}}(\Delta k_u,k_0,k) = {} & R_{SS}(\Delta k_u,k_0,k) + R_{NN}(\Delta k_u,k_0,k) \\ & + R_{SN}(\Delta k_u,k_0,k) + R_{NS}(\Delta k_u,k_0,k). \end{aligned} \tag{11}$$

Terms R_{SS} and R_{NN} denote the moving target and clutter-plus-noise autocorrelations, respectively. Terms R_{NS} and R_{SN} denote the crosscorrelations. The last three terms are expected to have insignificant values when compared with R_{SS}. As shown in (7), $|R_{SS}|$ displays a maximum for each k at $\Delta k_u = 2(k-k_0)\mu$. In order to have independent clutter samples, the sampling interval in the Fourier domain should be large enough (see (27) and (28) in Appendix A).

d) Perform a linear regression on the ordinates corresponding to the maximum values of $|R_{SS}|$ to estimate μ and subsequently compute the target slant-range velocity. As shown in Appendix B, the slant-range velocity estimation accuracy is proportional to the number of independent samples used to compute the linear regression.

The suggested scheme relies on the detectability of the moving targets. As shown in [14] the moving targets most hard to detect are those with cross-range velocity parallel to the platform motion (i.e., $\nu \leq 1$) and slant-range velocities inducing Doppler-shifts in the slow-time frequency domain such that the moving target spectrum completely overlaps the clutter spectrum. The moving target detection strategy proposed in step 1 of the algorithm works by filtering out the static ground echoes in the (k_u,k) frequency domain. The proposed scheme, in spite of being very simple, yields good results even for moving targets with slant-range velocities multiple of the Nyquist velocity, as far as the respective two-dimensional spectrum exhibits a nonnegligible skew.

In low SCR and low skew scenarios the moving target detection demands more sophisticated algorithms such as those proposed in [13], [14], [17], or [18], at expense of higher computational complexity. In [14] we have developed a moving target detection strategy that is able to detect moving targets in the case of parallel to platform target motion, the most unfavourable scenario, for SCR as low as 10 dB.

Notice that the suggested scheme does not require the knowledge of the parameters Y, α, or $A(k_u,k)$. It just needs an approximate value of X to estimate μ. This approximate value is given by

the slant-range position where the moving target is imaged after applying the moving target imaging (MTI) algorithm described in step 1. To estimate the cross-range velocity component of each moving target, we suggest the combination of the scheme herein proposed to estimate μ with the methodology presented by Soumekh in [1, ch. 6.7] to estimate $\alpha = \sqrt{\mu^2 + \nu^2}$. With the two quantities μ and α at hand, the estimation of ν is straightforward.

C. Computational Complexity

To evaluate the computational complexity of the proposed methodology, we follow a strategy similar to that presented in [19, ch. 12]. The approach consists in estimating the number of complex operations (C_{ops}) for each major step of the algorithm. A complex operation is defined as one radix-2 fast Fourier transform (FFT) butterfly, which consists of ten floating point operations (four floating point multiplications and six floating point additions). An equal cost for multiplications and additions is assumed. Accordingly to [19, ch. 12.2] and [20, ch. 15], the following C_{ops} are accounted:
FFT of size N: $C_{\text{fft}} \approx N/2 \log_2 N [C_{\text{ops}}]$;
2D FFT with dimension of N_x by N_y: $C_{fft2} \approx N_x N_y / 5 \log_2 N_x N_y [C_{\text{ops}}]$;
Complex multiplication: $C_m \approx 1 [C_{\text{ops}}]$;
Complex-by-real multiplication: $C_{mr} \approx 0.5 [C_{\text{ops}}]$;
2D linear interpolation with size of N_x by N_y: $C_p \approx 2 N_x N_y [C_{\text{ops}}]$.
The number of C_{ops} just accounted, slightly overestimates the total number of operations for a given algorithm. In this way we provide a margin for unaccounted machine cycles used in operations such as array index generation and memory access.

The algorithm herein proposed consists of the following main steps:

1) two runs of the wavefront reconstruction algorithm for a target area with N_x (slant-range) by N_y (cross-range) samples;
2) for each target:
a) a signature resynthesis for a spotlight region with N_{xs} (slant-range) by N_{ys} (cross-range) samples;
b) a correlation for each wavenumber in the resynthesized signature;
c) an auto-regression.

By summing the number of C_{ops} as described before, we obtain

$$C \approx 2N(2/5 \log_2 N + 1) + N_{\text{target}} \left[N_s \left(\frac{6}{5} \log_2 N_s + \frac{5}{2} \right) + \frac{\sqrt{N_s}}{10} (7 + \sqrt{N_s}) \right] [C_{\text{ops}}] \quad (12)$$

where $N \equiv N_x \times N_y$ and $N_s \equiv N_{xs} \times N_{ys}$; symbol N_{target} denotes the number of moving targets to process.

For step 2b we assumed N_{xs} correlations, each one of size N_{ys}. To obtain a simpler expression, we also considered $N_x = N_y$ and $N_{xs} = N_{ys}$.

As a numerical example, let us consider a target area of size $N = 1024 \times 1024$ pixels, containing $N_{\text{target}} = 100$ targets and that each digitally spotligthed region is of size $N_s = 20 \times 20$ pixels. In this situation, the algorithm requires 19.3 millions of C_{ops}, which is accomplished in less than half a second by a current desktop computer with a processor running at a clock speed of 1.5 GHz.

III. ESTIMATION RESULTS

The scheme proposed in the previous section is now applied to synthetic data and real data from the MSTAR public collection [21]. The synthetic data set contains seven moving targets, all with cross-range velocities several times above the Nyquist limit. The experiments with MSTAR data include clutter from Hunstville, Alabama and two BTR-60 transport vehicles with simulated movement.

A. Synthetic Data

The synthetic data set includes six point-like targets and an extended target with dimensions of 6 m in slant-range by 2 m in cross-range. The extended target is simulated by using twelve point-like targets, all with the same reflectivity. The SCR is set to 23 dB. The mission parameters are presented in Table I. The moving targets trajectory parameters are summarized in Table II. Targets numerated from one to six are point-like, whereas target number seven is extended. Coordinates x_0 and y_0 denote the moving targets positions when the SAR platform is at $u = 0$. The slant-range coordinates are recentered at the central slant-range coordinate x_c. The last column of this table displays the ratio between the moving target slant-range velocity magnitude $|v_x|$ and the maximum slant-range velocity allowed by the mission PRF, $v_{\max}$. Notice that all the moving targets have slant-range velocities several times larger than the Nyquist velocity. Fig. 3 shows the moving targets positions and their respective velocities. Each velocity vector is represented by an arrow with length proportional to the velocity magnitude.

Fig. 4 presents the target area image focused using the wavefront reconstruction algorithm [1] with static ground parameters. As expected, all the moving targets appear misplaced and blurred. To detect the moving targets we proceed as explained in the first step of the algorithm described in Section II. We start by applying high-pass filtering in the (k_u, k) domain with stop-band adjusted to filter out static targets. In the present situation this procedure consists in setting to zero the data inside the interval $-\pi/2 <$

TABLE I
Mission Parameters used in Simulation

Parameter	Value
Carrier frequency	9 GHz
Chirp bandwidth	250 MHz
Altitude	12 km
Velocity	637 km/h
Look angle	20°
Antenna radiation pattern	Raised Cosine
Oversampling factor (cross-range)	2
PRF	177 Hz

TABLE II
Moving Targets Parameters

Target	x_0 [m]	y_0 [m]	v_x [km/h]	v_y [km/h]	$\frac{\lvert v_x \rvert}{v_{\max}}$
1	−64	−64	−13.2	36	2.5
2	0	−64	−26.5	36	5
3	64	−64	−52.9	36	10
4	−64	+64	13.2	−36	2.5
5	0	+64	26.5	−36	5
6	64	+64	52.9	−36	10
7	0	0	52.9	0	10

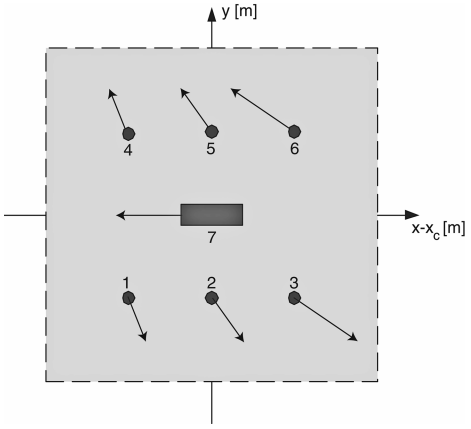

Fig. 3. Simulated positions and velocities of moving targets. Slant-range coordinates recentered at central slant-range coordinate x_c. Velocity vector of each target represented by arrow with length proportional to velocity magnitude.

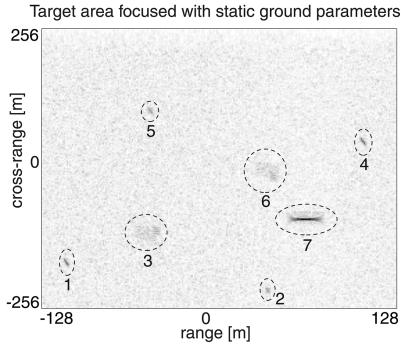

Fig. 4. Reconstructed SAR image with static ground parameters. Moving targets appear defocused and misplaced.

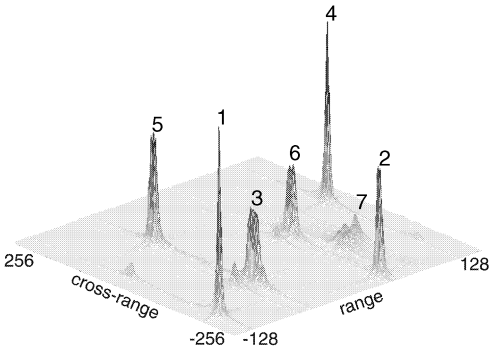

Fig. 5. MTI function after static ground filtering.

$k_u < \pi/2$ [rad/m]. We then perform imaging using the wavefront reconstruction algorithm with static ground parameters. The resulting MTI function is presented in Fig. 5, where we can see that all moving targets are clearly detectable.

For illustration purposes, we show in Fig. 6(a) and Fig. 7(a) the magnitude of the digitally spotlighted signatures of point-like target 3 and extended target 7, respectively.

In Fig. 6(b) and Fig. 7(b) we show the resulting data after performing the proposed correlation. A straight line is clearly visible in both figures, although in the case of the moving target 7 the interaction between the multiple scatterers that compose the object causes the amplitude to fluctuate. The slope of the resulting lines is estimated by means of a linear regression. Table III presents the slant-range velocity estimates for all the moving objects in the scene. The accuracy is better than 1% for all targets and can be used to retrieve the true Doppler interval where the moving target signature belongs to.

To estimate the full velocity vector we combined the unaliased estimates of the slant-range velocity obtained herein with the estimates of the relative speed α measured as proposed by Soumekh in [1, ch. 6.7]. Table IV presents the resulting full velocity vector estimates, illustrating the usefulness of this method. The accuracy is better than 2% with respect to the velocity vector norm.

B. Real Data

In this subsection we apply the proposed strategy to real data from the MSTAR public collection. The clutter scene is taken from Huntsville, Alabama. The moving objects are two BTR-60 transport vehicles with simulated movement. The optical and X-band images of this type of vehicle are presented in Fig. 8.

The nth moving target signature was generated, according to (2), by computing

$$S_{mn}(k_u,\omega) = \sum_i A_n(k_u,k)P(\omega)f_{in}e^{-j\sqrt{4k^2-(k_u/\alpha_n)^2}X_{ik}+(k_u/\alpha_n)Y_{ik}} \tag{13}$$

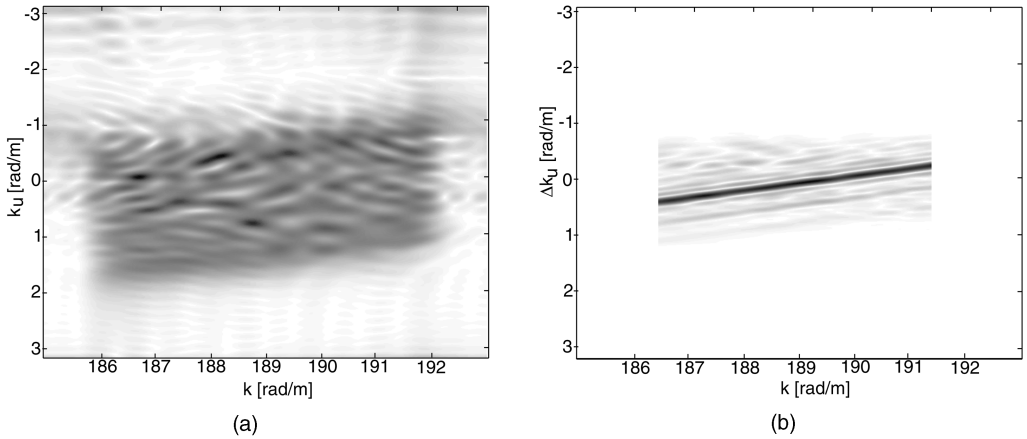

Fig. 6. (a) Moving target 3 signature in (k_u,k) domain after digital spotlight operation. (b) Maximum of proposed correlation changes linearly with fast-time frequency as predicted.

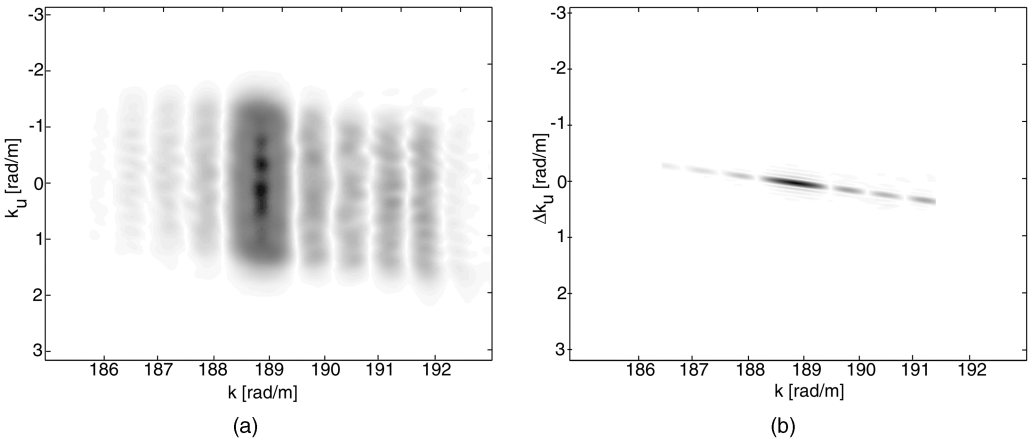

Fig. 7. (a) Extended moving target 7 signature in (k_u,k) domain after digital spotlight operation. (b) Result from proposed correlation. Maximum exhibits fluctuation due to interaction between multiple scatterers that compose object.

TABLE III
Slant-Range Velocity Estimation Results (SCR = 23 dB)

Target	v_x [km/h]	$\hat{v}_x$ [km/h]	Error
1	−13.2	−13.25	0.4%
2	−26.5	−26.69	0.6%
3	−52.9	−53.21	0.6%
4	13.2	13.24	0.3%
5	26.5	26.26	0.9%
6	52.9	52.5	0.7%
7	52.9	53.03	0.3%

TABLE IV
Complete Velocity Vector Estimation by Joining Two Methodologies (SCR = 23 dB)

Target	(v_x,v_y) [km/h]	$(\hat{v}_x,\hat{v}_y)$ [km/h]
1	(−13.2,36)	(−13.25,35.53)
2	(−26.5,36)	(−26.69,35.78)
3	(−52.9,36)	(−53.21,32.9)
4	(13.2,−36)	(13.24,−32)
5	(26.5,−36)	(26.26,−38.8)
6	(52.9,−36)	(52.5,−37.33)
7	(52.9,0)	(53.03,1.54)

where indexes i and n denote the ith pixel of the nth moving target. Function A_n is the two-way antenna radiation pattern for the nth moving target given by (3).

The mission parameters for the MSTAR data are presented in Table V. Table VI details the moving targets velocities and coordinates. The SCR is roughly set to 23 dB. Notice that the slant-range velocities of both targets induce Doppler-shifts corresponding to 6 and 12 times the maximum unambiguous value imposed by the PRF. The resulting data was focused using the wavefront reconstruction algorithm with static ground parameters. The obtained image is presented in Fig. 9, where the moving objects appear defocused and misplaced as expected.

Each moving object signature was digitally spotlighted in the spatial domain and resynthesized back to the (k_u,k) frequency domain as proposed in [13]. The resulting resynthesized signature in the (k_u,k) domain is presented in Fig. 10 for illustration purposes only.

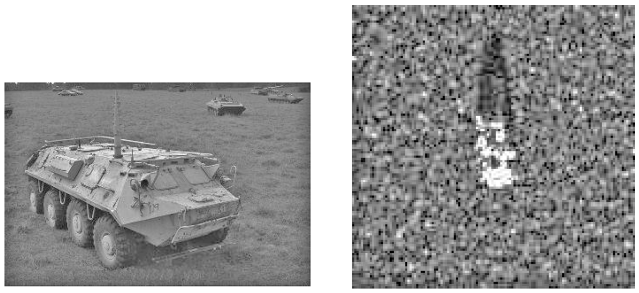

(a) (b)

Fig. 8. BTR-60 transport vehicle. (a) Optical. (b) X-band.

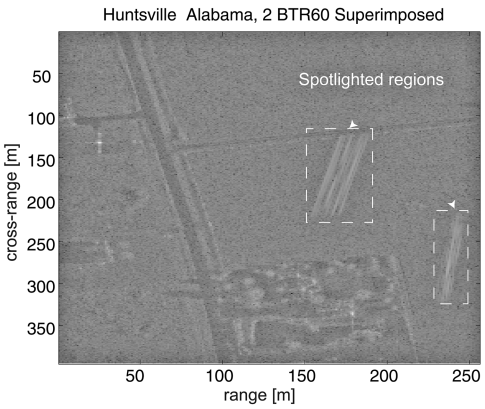

Fig. 9. Scene from Hunstville, Alabama, where two moving BTR-60 transport vehicles are superimposed. Slant-range velocity of vehicle on left exceeds Nyquist limit by 6 times. Vehicle on right exceeds that velocity by 12 times. They appear defocused and misplaced as expected.

TABLE V
Real Data Mission Parameters

Parameter	Value
Carrier frequency	9.6 GHz
Chirp bandwidth	250 MHz
Altitude	12 km
Velocity	637 km/h
Look angle	15°
Antenna radiation pattern	Raised Cosine
Oversampling factor (cross-range)	2
PRF	177 Hz

TABLE VI
BTR-60 Transport Vehicle Trajectory Parameters

Target	x_0 [m]	y_0 [m]	v_x [km/h]	v_y [km/h]	$\frac{\lvert v_x \rvert}{v_{\max}}$
1	75	220	29.85	−36	6
2	180	122	59.69	−7.2	12

The maximum magnitude of correlation (7) is shown in Fig. 11(b). It varies linearly with the fast-time frequency as predicted, although exhibiting local correlation due to the interaction between the large number of scatterers that compose the BTR-60 vehicle. Nevertheless, the resulting velocity estimates are still very accurate (see Table VII).

As we did in the previous subsection, we used both estimates of μ and α to retrieve the full velocity vector. Table VIII shows the obtained results. The accuracy with respect to the estimation of the velocity vector norm is better than 4%.

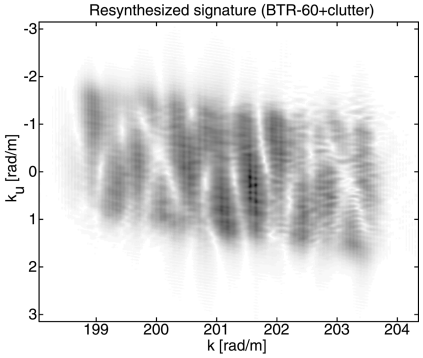

Fig. 10. Resynthesized signature of the BTR-60 plus clutter.

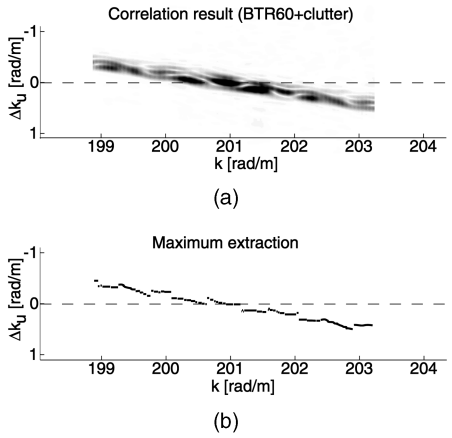

Fig. 11. (a) Result of proposed correlation for BTR-60 vehicle moving with slant-range velocity of 12 times the maximum imposed by mission PRF. (b) Ordinates where maximum values of previous correlation occur. True slant-range velocity retrieved with error of 2.6%.

TABLE VII
Slant-Range Velocity Estimation Results (SCR = 23 dB)

Target	v_x [km/h]	$\hat{v}_x$ [km/h]	Error
1	29.85	29.05	2.7%
2	59.69	61.24	2.6%

TABLE VIII
Complete Velocity Vector Estimation (SCR = 23 dB)

Target	(v_x, v_y) [km/h]	$(\hat{v}_x, \hat{v}_y)$ [km/h]
1	(29.85, −36)	(29.05, −38.91)
2	(59.69, −7.2)	(61.24, −8.21)

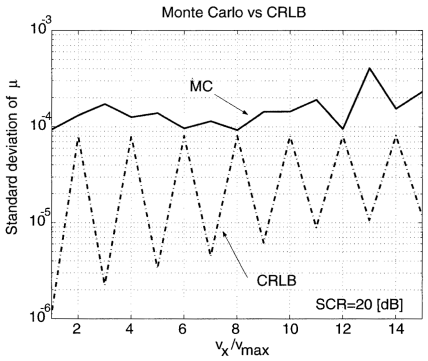

Fig. 12. Monte Carlo results (64 runs) versus Cramer-Rao Bound.

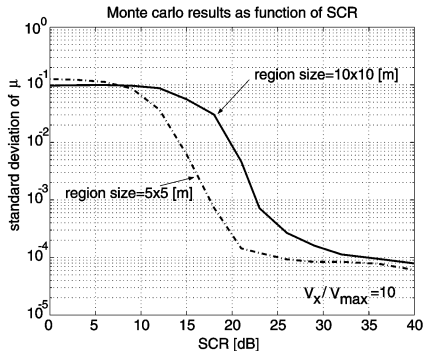

Fig. 13. Monte Carlo results (64 runs) as function of SCR.

C. Monte Carlo Results

Fig. 12 plots the standard deviation of μ obtained by Monte Carlo estimation (64 runs) and the Cramer-Rao lower bound (CRLB) given by the right-hand side of (42), versus the normalized cross-range velocity $v_x/v_{\max}$. The digitally spotlighted region size is 5×5 [m], the number of independent samples is $M = 5$, and the SCR is 20 dB. The mission parameters are listed in Table I.

The CRLB exhibits a periodic type pattern due to the overlapping of the moving object spectrum on the clutter spectrum when $v_x/v_{\max}$ is even. When the ratio $v_x/v_{\max}$ is odd, the overlapping is minimum and we can expect better estimation results. As can be seen, the presented strategy performs quite well, although it does not reach the CRLB. Notice that the Monte Carlo results do not present the periodic shape of the CRLB curve. This is due to the fact that the proposed estimator, which is based on a correlation, does not include any information about the clutter statistics. If we had used the clutter covariance matrix in the derivation of the estimator, we should have had the periodic behavior present on the CRLB curve and a smaller offset between the CRLB curve and the Monte Carlo results. However, the estimator would be more complex and less robust, as it would depend on the antenna radiation pattern which, usually, is not precisely known.

Fig. 13 plots Monte Carlo results, for a fixed $v_x/v_{\max} = 10$, as function of the SCR. The dashed curve considers a spotlight region with dimensions of 5×5 [m] and the solid curve refers to a spotlight region with dimensions of 10×10 [m]. For SCR below 6 dB, the estimator gives useless results, since the estimation errors are much larger than the Nyquist limit given by $\mu_{\max} = v_{\max}/V = \lambda_0 \mathrm{PRF}/(4V) = 0.0083$. For SCR between 6 dB and 25 dB, the estimator accuracy increases with the SCR. If we define as minimum requirement that the standard deviation of μ must be smaller than the Nyquist limit, i.e., $\sigma_\mu < 0.0083$, then we can see that the estimator gives effective results for SCR $>$ 14 dB for the dashed curve and SCR $>$ 20 dB for the solid curve. For SCR above 25 dB the estimator accuracy is almost constant and close to the CRLB.

Concerning the larger spotlight region, and for 6 dB$\leq$ SCR $\leq$ 25 dB, we can read a degradation of approximately 6 dB for the minimum requirement. This degradation is to be expected, because the second digitally spotlighted region has 4 times the area of the first region and the estimator does not use any information about the clutter statistics. As a rule of thumb, for each quadrupling of the spotlight area, we can expect a degradation of, approximately, 6 dB on the minimum SCR required.

D. Violation of Assumptions

The proposed methodology to obtain the slant-range velocity of the moving targets relies on the following assumptions.

1) The reflectivity of moving targets is independent of the aspect angle.
2) The moving targets are point-like or they contain predominant scatterers, thus exhibiting point-like behavior.
3) The moving targets are separable from each other in the spatial domain.
4) The clutter that remains after the digital spotlight operation exhibits small correlation in the frequency domain.

The first assumption greatly simplifies the problem formulation and yet leads to good results. The second assumption is reasonable, as most man-made targets can be considered to be a set of individual point-like scatterers [22]. In this subsection we illustrate what happens when the assumptions 3 and 4 are violated. We start with the analysis of a scenario where two moving targets appear overlapped in the unfocused image. In this situation the digital spotlight operation cannot isolate one target from the other. The resynthesized signature of the spotlighted region can thus be written as

$$\hat{S}_m(k_u,k) = S_{m1}(k_u,k) + S_{m2}(k_u,k) + S_{0R}(k_u,k) \quad (14)$$

where S_{m1} and S_{m2} are the signatures of the two moving targets and S_{0R} is the remaining noise after the digital spotlight operation.

The correlation $R_{\hat{S}\hat{S}}$ between $\hat{S}_m(k_u,k_0)$ and $\hat{S}_m(k_u,k)$ is

$$\begin{aligned} R_{\hat{S}\hat{S}}(\Delta k_u,k_0,k) &= R_{S1S1}(\Delta k_u,k_0,k) + R_{S2S2}(\Delta k_u,k_0,k) \\ &\quad + R_{S1S2}(\Delta k_u,k_0,k) + R_{S2S1}(\Delta k_u,k_0,k) \\ &\quad + R_0(\Delta k_u,k_0,k) \end{aligned} \tag{15}$$

where

$$\begin{aligned} R_0(\Delta k_u,k_0,k) &= R_{S1N}(\Delta k_u,k_0,k) + R_{S2N}(\Delta k_u,k_0,k) \\ &\quad + R_{NS1}(\Delta k_u,k_0,k) + R_{NS2}(\Delta k_u,k_0,k) \\ &\quad + R_{NN}(\Delta k_u,k_0,k). \end{aligned} \tag{16}$$

Terms R_{S1S1} and R_{S2S2} denote the autocorrelation of each moving target signature. Terms R_{S1S2} and R_{S2S1} denote their crosscorrelations. Term R_0 contains the crosscorrelations between each moving target signature and the remaining clutter. Term R_{NN} is the autocorrelation of the remaining clutter.

As shown in (7), each R_{SiSi} originate maxima with slope depending on the respective moving target relative slant-range velocity. Terms contained in R_0 are expected to have negligible values, when compared with the autocorrelation of each of the moving targets. We now focus on the remaining two terms corresponding to the crosscorrelations between the moving targets. Following a procedure similar to that used to derive (7), we obtain

$$\begin{aligned} &R_{SiSj}(\Delta k_u,k_1,k_1+\Delta k) \\ &\quad \propto \int_{-\infty}^{+\infty} A_i(k_u,k_1)A_j^*(k_u-2\Delta k\mu_j-\Delta k_u,k_1)e^{j\phi_j}dk_u \end{aligned} \tag{17}$$

where $i,j = 1,2$ $(i \neq j)$ indexes terms corresponding to the respective moving target, and

$$\phi_j \approx \frac{2k_u\Delta k_u}{4(k_1+\Delta k)\alpha_j^2}X_j + \frac{k_u^2}{4k_1}\left(\frac{X_i}{\alpha_i^2}-\frac{X_j}{\alpha_j^2}\right) + k_u\left(\frac{Y_i}{\alpha_i}-\frac{Y_j}{\alpha_j}\right). \tag{18}$$

When compared with (8), phase ϕ_j depends also on the differences between the moving targets motion transformed coordinates. The most important term of (18) is $k_u(Y_i/\alpha_i - Y_j/\alpha_j) \approx k_u(Y_i - Y_j)$. Roughly, if $|Y_i - Y_j| > \pi/B_u$, we can expect (17) to have insignificant values when compared with the autocorrelation of each of the moving targets. For the mission parameters given in Table I this implies that differences larger than, approximately, 1[m], are sufficient to make the crosscorrelation terms negligible. Therefore, if the digitally spotlighted region contains two moving targets with different velocities, it can be expected that the proposed correlation will produce two lines, resulting from the autocorrelation terms R_{S1S1} and R_{S2S2}, with slopes corresponding to each moving target slant-range velocity.

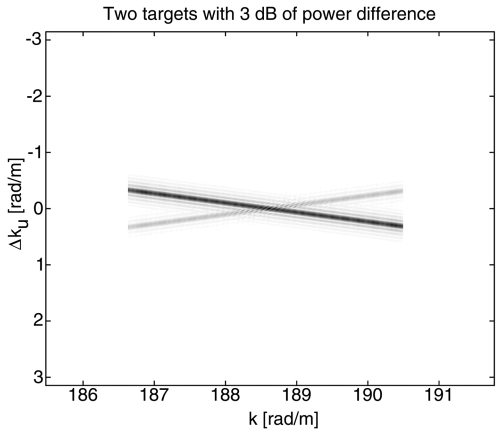

Fig. 14. Result of proposed correlation in scenario where two moving objects with different reflectivities and opposite slant-range speeds are present. As expected, result is two lines with distinct intensities and symmetric slopes.

The previous analysis is now illustrated using simulated data. We start with a scenario containing two point-like moving targets with velocity vectors of targets 1 and 3 listed in Table II. Their slant-range velocities are 10 times greater than $v_{\max}$, but they travel in opposite directions. Both targets were simulated to appear overlapped in the unfocused image and the difference $|Y_i - Y_j|$ is 7[m]. One of the targets has reflectivity 3 dB greater than the other. In this case the digital spotlight operation cannot isolate one target from the other. Both signatures will thus be used simultaneously in the computation of the correlation (7). The correlation result is shown in Fig. 14, where two lines with different intensities and symmetric slopes are clearly distinguishable. Each line corresponds to one moving target. The intensities are distinct due to the different reflectivity of each moving target.

In the next example the assumption of small correlation for the clutter is violated. To accomplish this, we superimpose a moving target on a man-made structure after focusing the target area with static ground parameters. The considered man-made structure is positioned at coordinates (131,39) (see Fig. 9). The digital spotlight operation is not able to separate the two objects, and the signature of the static structure will be used in the correlation. Conceptually, this structure can be thought of as a moving target with zero velocity. Therefore, we may expect a horizontal line due to it. The correlation result is presented in Fig. 15, where two lines with different slopes are clearly visible. As predicted, the horizontal line is due to the static man-made structure. The line with non-zero slope is originated by the moving target.

From the previous examples we see that we cannot simply apply the last step of the proposed

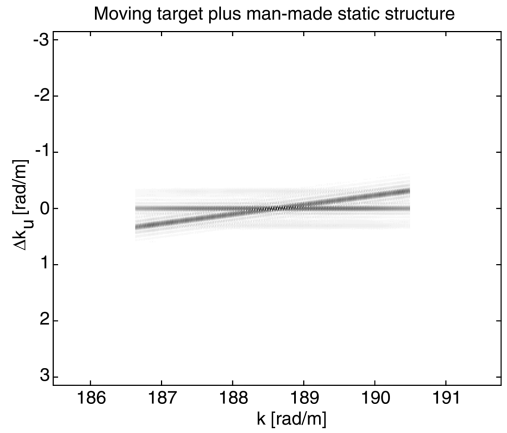

Fig. 15. Result of proposed correlation in scenario where digital spotlight operation is not able to separate moving object from a man-made static structure. Resulting horizontal line is due to static structure. Off-horizontal line due to moving object.

algorithm, which consists on a linear regression on the correlation maxima. A more sophisticated scheme is thus necessary. We will address these scenarios in the near future.

IV. CONCLUSIONS AND FINAL REMARKS

This paper presents a novel methodology to retrieve unaliased estimates of the slant-range velocity of moving targets inducing Doppler-shifts beyond the Nyquist limit imposed by the mission PRF. The methodology exploits the linear dependency of the Doppler-shift with the slant-range velocity for each fast-time frequency. That is, the echo from a moving object, in the two-dimensional frequency domain, exhibits a skew not subject to PRF limitations. An estimator of the spectrum skew is proposed and its usefulness using real and synthetic data is illustrated. The accuracy is shown to depend on the transmitted pulse bandwidth. Basically, this is due to the fact that by using a larger bandwidth we have a larger number of independent samples to feed the estimator and, therefore, we have lower variance on the resulting velocity estimates. The method gives effective results even when the returned echoes of the moving targets and the static ground overlap completely, provided that the moving targets signatures are digitally spotlighted and the SCR is greater than 14 dB.

By combining the methodology herein proposed with an existing algorithm to retrieve the velocity vector magnitude, the full velocity vector is estimated with high accuracy using aliased data from a single SAR sensor.

The major limitations of the proposed approach are the following assumptions:

1) The reflectivity of moving targets is independent of the aspect angle.

2) The moving targets are point-like or they contain predominant scatterers, thus exhibiting approximately point-like behavior.

3) The moving targets are separable from each other in the spatial domain.

4) The clutter that remains after the digital spotlight operation exhibits small correlation in the frequency domain.

The first assumption greatly simplifies the problem formulation and yet leads to good results. The second assumption is reasonable as most man-made targets can be considered to be a set of individual point-like scatterers [22]. We then consider the problems that arise when the last two assumptions are violated. We derive theoretically the correlation structure when two moving targets are not separable in the spatial domain. In this scenario, the correlation will result in two maxima with slopes depending on each moving target relative slant-range velocity.

The last assumption is also theoretically addressed, in the situation where the digitally spotlighted region contains a moving target and a man-made structure. In this situation, the correlation shows two maxima, one of them occurring for $\mu = 0$ (a horizontal line). The horizontal line is due to the man-made structure and the off-horizontal line is due to the moving target. These theoretically derived results are confirmed by simulations.

APPENDIX A. GROUND RETURNS COVARIANCE IN SLOW-TIME AND FAST-TIME FREQUENCY DOMAINS

In this section we show that the covariance of the echoes returned from the static ground in the slow-time and fast-time frequency domains decays very quickly, if we consider the clutter to be homogeneous with a large number of scatterers per resolution cell.

The returned echo from the static ground can be written as [1, 14, 23]

$$S(k_u,k) = |P(\omega)|^2 A(k_u,\theta_0) \sum_n f_n e^{-j\xi_n(k_u,k)} \qquad (19)$$

where f_n is the reflectivity of the nth static scatterer with coordinates (x_n,y_n), symbol $\theta_0 \equiv (\mu_0,\nu_0) = (0,1)$, and

$$\xi_n(k_u,k) \equiv \sqrt{4k^2 - k_u^2}\,x_n + k_u y_n. \qquad (20)$$

The covariance of S, $C_S(k_{u_1},k_{u_2},k_1,k_2) \equiv E[S(k_{u_1},k_1)S^*(k_{u_2},k_2)]$, is therefore

$$\begin{aligned} &C_S(k_{u_1},k_{u_2},k_1,k_2) \\ &\quad = E\left[|P(\omega_1)|^2 |P(\omega_2)|^2 A(k_{u_1},\theta_0) A^*(k_{u_2},\theta_0) \right. \\ &\qquad \left. \times \sum_n f_n e^{-j\xi_n(k_{u_1},k_1)} \sum_m f_m^* e^{j\xi_m(k_{u_2},k_2)} \right]. \end{aligned} \qquad (21)$$

If the scatterers are mutually independent, and each one has a phase independent of its amplitude and uniformly distributed in a 2π, interval , then $E[f_n f_m^*] = 0$ if $n \neq m$, and $E[f_n f_m^*] \equiv \sigma_n$ if $n = m$. The covariance is therefore written as

$$C_S(k_{u_1},k_{u_2},k_1,k_2) = \underbrace{|P(\omega_1)^2||P(\omega_2)^2|A(k_{u_1},\theta_0)A^*(k_{u_2},\theta_0)}_{\Gamma(k_{u_1},k_{u_2},k_1,k_2)} \times \sum_n \sigma_n e^{-j[\xi_n(k_{u_1},k_1)-\xi_n(k_{u_2},k_2)]}. \quad (22)$$

Using the approximation $\sqrt{4k^2-k_u^2} \approx 2k-(k_u^2/4k)$, valid for $k \gg k_u$, we get

$$C_S(k_{u_1},k_{u_2},k_1,k_2) \approx \Gamma(k_{u_1},k_{u_2},k_1,k_2) \times \sum_n \sigma_n e^{-2j(k_1-k_2-(k_{u_1}^2/8k_1)+(k_{u_2}^2/8k_2))x_n} e^{-j(k_{u_1}-k_{u_2})y_n}. \quad (23)$$

Let us consider a homogeneous scene with constant backscattering coefficient given by

$$\sigma_0 = \frac{1}{\Delta} \sum_{n:(x_n,x_n)\epsilon\Delta(x',y')} \sigma_n \quad (24)$$

where $\Delta(x',y')$ is a small rectangle of area Δ centered at (x',y'). Expression (23) can thus be approximated by

$$C_S(k_{u_1},k_{u_2},k_1,k_2) \approx \Gamma(k_1,k_2,k_{u_1},k_{u_2})\sigma_0 \times \int_{-L_x/2}^{L_x/2}\int_{-L_y/2}^{L_y/2} e^{-j2(k_1-(k_{u_1}^2/8k_1)-k_2+(k_{u_2}^2/8k_2))x} e^{j(k_{u_1}-k_{u_2})y} dx\,dy \quad (25)$$

where L_x and L_y are the target area lengths in slant-range and cross-range directions, respectively. After some algebraic transformation we are lead to

$$C_S(k_{u_1},k_{u_2},k_1,k_2) \approx \Gamma(k_{u_1},k_{u_2},k_1,k_2)\sigma_0 L_x L_y \times \operatorname{sinc}\left[\frac{k_{u_1}-k_{u_2}}{2\pi}L_y\right] \times \operatorname{sinc}\left[\frac{\left(\left(k_1-\frac{k_{u_1}^2}{8k_1}\right)-\left(k_2-\frac{k_{u_2}^2}{8k_2}\right)\right)}{\pi}L_x\right]. \quad (26)$$

Larger values of L_x and L_y lead to more localized mainlobes of the sinc functions. In the slow-time frequency axis the covariance C_s is null for

$$|k_{u_1}-k_{u_2}| = \frac{2\pi}{L_y} \quad (27)$$

and in the fast-time frequency axis the covariance is zero for

$$|k_1-k_2| = \frac{\pi}{L_x}. \quad (28)$$

Under the large number of scatterers per resolution cell assumption, $S(k_u,k)$ is Gaussian (see Appendix B). Therefore, samples of $S(k_u,k)$ are independent if they are taken with spacing given by (27) and (28).

APPENDIX B. THEORETICAL BOUNDS

In this section we compute the CRLB for the velocity components of moving targets.

As we saw previously, the returned echo from the static ground after pulse compression is

$$S_0(k_u,\omega) = |P(\omega)|^2 A(k_u,\theta_0)\sum_n f_n e^{-\xi_n(k_u,\omega)} \quad (29)$$

where

$$\xi_n(k_u,\omega) = \sqrt{4k^2-k_u^2}x_n + k_u y_n \quad (30)$$

and $\theta_0 = (\mu_0,\nu_0) = (0,1)$ denotes the velocity vector parameters for the static ground. For a point-like moving target with motion transformed coordinates (X,Y) and complex reflectivity f_m, the echoed signal is [1, 14]

$$S_m(k_u,\omega) = |P(\omega)|^2 A(k_u,\theta) f_m e^{-\xi_m(k_u,\omega,\alpha)} \quad (31)$$

where $\alpha = \sqrt{\mu^2+\nu^2}$ and $\theta = (\mu,\nu)$ and

$$\xi_m(k_u,\omega,\alpha) = \sqrt{4k^2-(k_u/\alpha)^2}X + (k_u/\alpha)Y. \quad (32)$$

The total echo returned due to the static ground and the moving target is thus

$$(k_u,\omega) = S_0(k_u,\omega) + S_m(k_u,\omega). \quad (33)$$

Let us define the vector

$$\mathbf{S} \equiv [S_{-N}\cdots S_0\cdots S_N]^T \quad (34)$$

for a fixed fast-time frequency ω_c, where $S_i \equiv S(k_{u_i},\omega_c)$, $k_{u_i} = (i/2N)\Delta K$ for $i = -N,\ldots,N$, and symbol ΔK denotes the spatial sampling frequency. In order to have independent samples, the sampling frequency ΔK is selected according to expression (28). Define also $\mathbf{A}(\theta) \equiv [A_{-N}(\theta)\cdots A_0(\theta)\cdots A_N(\theta)]^T$, where $A_i(\theta) \equiv A(k_{u_i},\theta)$.

Let us assume that the number of static scatterers per resolution cell is large, none is predominant, the echo amplitudes f_n are mutually independent and each one has a phase independent of its amplitude which is uniformly distributed in a 2π interval. Then, the vector $\mathbf{S}$ is complex circular zero-mean and Gaussian [24]. The density of vector $\mathbf{S}$ conditioned to θ and the target reflectivity can thus be written as

$$p(\mathbf{S} \mid f_m,\theta) = \frac{1}{2\pi^N|\mathbf{C}_s|} e^{-(\mathbf{S}-\mathbf{m}_s)^H\mathbf{C}_s^{-1}(\mathbf{S}-\mathbf{m}_s)} \quad (35)$$

where the mean $\mathbf{m}_s$ is given by

$$\mathbf{m}_s \equiv f_m |P(\omega_c)|^2 \mathbf{A}(\theta)\mathbf{Q} \tag{36}$$

and $\mathbf{Q} \equiv \text{diag}[e^{-j\xi_m(k_{u_i},\omega_c,\alpha)},\ i = -N,\ldots,N]$.

As already shown in the previous appendix, the inverse of the covariance matrix $\mathbf{C}_s$ is given by

$$\mathbf{C}_s^{-1} = \frac{1}{|P(\omega_c)|^4 \sigma_0 L_x L_y} \text{diag}[|A(k_{ui},\theta_0)|^{-2},\ i = -N,\ldots,N]. \tag{37}$$

The elements of the Fisher information matrix for a circular complex Gaussian process are given by [24]

$$[I(\boldsymbol{\theta})]_{ij} = \text{tr}\left[\mathbf{C}_s^{-1}(\boldsymbol{\theta})\frac{\delta \mathbf{C}_s(\boldsymbol{\theta})}{\delta\theta_i}\mathbf{C}_s^{-1}(\boldsymbol{\theta})\frac{\delta \mathbf{C}_s(\boldsymbol{\theta})}{\delta\theta_j}\right] + 2\text{Re}\left[\frac{\delta \mathbf{m}_s^H(\boldsymbol{\theta})}{\delta\theta_i} C_s^{-1}(\boldsymbol{\theta})\frac{\delta \mathbf{m}_s(\boldsymbol{\theta})}{\delta\theta_j}\right], \quad i,j = 1,2. \tag{38}$$

The first term in (38) is null because the noise covariance matrix is independent of the moving target parameters. After some lengthy algebraic transformation we achieve the following expressions for the Fisher matrix elements:

$$I_{11}(\theta) = \frac{2|f_m|^2}{\sigma_0 L_x L_y}\left[\sum_i \frac{|A_i(\theta)|^2}{|A_i(\theta_0)|^2} k_{ui}^2 \mu^2 \times \left(\frac{k_{ui} X}{\alpha^2\sqrt{4k^2 - (k_{ui}/\alpha)^2}} - \frac{Y}{\alpha^3}\right)^2 + \frac{k^2}{\nu^2}\sum_i \frac{|\dot{A}_i(\theta)|^2}{|A_i(\theta_0)|^2}\right] \tag{39}$$

$$I_{12}(\theta) = I_{21}(\theta) = \frac{|f_m|^2}{\sigma_0 L_x L_y}\left[2\mu\nu\sum_i \frac{|A_i(\theta)|^2}{|A_i(\theta_0)|^2} k_{ui}^2 \times \left(\frac{k_{ui} X}{\alpha^2\sqrt{4k^2 - (k_{ui}/\alpha)^2}} - \frac{Y}{\alpha^3}\right)^2 + \frac{k}{\nu^3}\sum_i (k_{ui} - 2k\mu)\frac{|\dot{A}_i(\theta)|^2}{|A_i(\theta_0)|^2}\right] \tag{40}$$

$$I_{22}(\theta) = \frac{|f_m|^2}{2\sigma_0 L_x L_y}\left[4\nu^2\sum_i \frac{|A_i(\theta)|^2}{|A_i(\theta_0)|^2} k_{ui}^2 \times \left(\frac{k_{ui} X}{\alpha^2\sqrt{4k^2 - (k_{ui}/\alpha)^2}} - \frac{Y}{\alpha^3}\right)^2 + \frac{(k_{ui} - 2k\mu)^2}{\nu^4}\sum_i (k_{ui} - 2k\mu)\frac{|\dot{A}_i(\theta)|^2}{|A_i(\theta_0)|^2}\right]. \tag{41}$$

The Cramer-Rao Bounds for μ and ν are given by the inverse of the Fisher Information matrix (principal diagonal elements), that is, $\text{CRLB}(\mu) = [I^{-1}(\theta)]_{11}$ and $\text{CRLB}(\nu) = [I^{-1}(\theta)]_{22}$.

The proposed estimator uses several measurements on the available pulse bandwidth. If we consider that the measurements are independent and the CRLB has small variation on the frequency interval $k \in [-\pi B/c + k_0, k_0 + \pi B/c]$, we have then

$$\sigma_\mu^2 \le \frac{1}{M}[I^{-1}(\theta)]_{11} \tag{42}$$

where M is the number of independent measurements taken in the available pulse bandwidth. On the other hand, the estimator proposed here is based on the linear regression of the correlation maxima occurring at $k_{u_i} = 2\mu(k_i - k_0) + \varepsilon_i$, where ε_i is a random variable with variance, say, σ_ε^2. A simple but lengthy algebraic computation leads to the conclusion that

$$\sigma_\mu^2 \approx \frac{3}{M}\frac{\sigma_\varepsilon^2}{K^2} \tag{43}$$

with $K = 2\pi B/c$.

This result states that the accuracy of the slant-range velocity estimates increases by augmenting the number of independent observations and by enlarging the transmitted pulse bandwidth. In Section III of the main text we plot CRLB curves and compare these with the results obtained via Monte Carlo simulations.

ACKNOWLEDGMENTS

The authors acknowledge the Air Force Research Laboraty (AFRL) and the Defense Advanced Research Projects Agency (DARPA) for the MSTAR data they promptly made available.

REFERENCES

[1] Soumekh, M.
Synthetic Aperture Radar Signal Processing with MATLAB Algorithms.
New York: Wiley-Interscience, 1999.

[2] Raney, R.
Synthetic aperture imaging radar and moving targets.
IEEE Transactions on Aerospace and Electronic Systems, **AES-7** (1971), 499–505.

[3] Marques, P., and Dias, J.
Optimal detection and imaging of moving objects with unknown velocity.
In *Proceedings of the 3rd European Conference on Synthetic Aperture Radar* (EUSAR 2000), 2000, 561–564.

[4] Barbarossa, S., and Farina, A. (1994)
Space-time-frequency processing of synthetic aperture radar signals.
IEEE Transactions on Aerospace and Electronic Systems, **30** (Apr. 1994), 341–358.

[5] Freeman, A., and Currie, A.
Synthetic aperture radar (SAR) images of moving targets.
GEC Journal of Research, **5** (1987), 106–115.

[6] Wang, G., Xia, X., Chen, V., and Fiedler, R.
Detection, location and imaging of fast moving targets using multi-frequency antenna array SAR (MF-SAR).
In *Proceedings of the 3rd European Conference on Synthetic Aperture Radar* (EUSAR 2000), 2000, 557–560.

[7] Barbarossa, S.
Detection and imaging of moving objects with synthetic aperture radar.
IEE Proceedings Pt. F, **139** (Feb. 1992), 79–88.

[8] Legg, J., Bolton, A., and Gray, D.
SAR moving target detection using non-uniform PRI.
In *Proceedings of the 1st European Conference on Synthetic Aperture Radar* (EUSAR'96), 1996, 423–426.

[9] Xia, S.
On estimation of multiple frequencies in undersampled complex valued waveforms.
IEEE Transactions on Signal Processing, **47** (Dec. 1999), 3417–3419.

[10] Kirscht, M.
Detection and imaging of arbitrarily moving targets with single-channel SAR.
In *Proceedings of the RADAR 2002*, Edinburg, UK, Oct. 2002, 280–285.

[11] Marques, P., and Dias, J.
Moving targets velocity estimation using aliased SAR raw-data from a single sensor.
In *Proceedings of the 4th European Conference on Synthetic Aperture Radar* (EUSAR 2002), Cologne, Germany, June 2002, 389–392.

[12] Bamler, R., and Runge, H.
PRF-ambiguity resolving by wavelength diversity.
IEEE Transactions on Geoscience and Remote Sensing, **29** (Nov. 1991), 997–1003.

[13] Soumekh, M.
Reconnaissance with ultra wideband UHF synthetic aperture radar.
IEEE Signal Processing Magazine, (July 1995), 21–40.

[14] Dias, J., and Marques, P.
Moving targets detection and trajectory parameters estimation using a single SAR sensor.
IEEE Transactions on Aerospace and Electronic Systems, **39** (Apr. 2003), 604–624.

[15] Ender, J.
The airborne experimental multi-channel SAR-system AER-II.
In *Proceedings of the 1st European Conference on Synthetic Aperture Radar* (EUSAR'96), 1996, 49–52.

[16] Blacknell, D.
Target detection in correlated SAR clutter.
IEEE Proceedings on Radar, Sonar and Navigation, **147** (Feb. 2000), 9–16.

[17] Ender, J.
Detection and estimation of moving target signals by multi-channel SAR.
In *Proceedings of the 1st European Conference on Synthetic Aperture Radar* (EUSAR'96), 1996, 411–417.

[18] Fienup, J.
Detecting moving targets in SAR imagery by focusing.
IEEE Transactions on Aerospace and Electronic Systems, **37** (July 2001), 794–809.

[19] Carrara, W., Goodman, R., and Majewski, R.
Spotlight Synthetic Aperture Radar: Signal Processing Algorithms.
Dedham, MA: Artech House, 1995.

[20] Kay, S.
Modern Spectral Estimation.
Englewood Cliffs, NJ: Prentice-Hall, 1988.

[21] Ross, T., Worrell, S., Velten, V., Mossing, J., and Bryant, M.
Standard SAR ATR evaluation experiments using the MSTAR public release data set.
In *SPIE Proceedings: Algorithms for Synthetic Aperture Radar Imagery V*, 1998, 566–573.

[22] Chen, V., and Ling, H.
Joint time-frequency analysis for radar signal and image processing.
IEEE Signal Processing Magazine, **16** (Mar. 1999), 81–93.

[23] Marques, P., and Dias, J.
Moving targets in synthetic aperture images: A Bayesian approach.
In *Proceedings of the International Conference on Image Processing* (ICIP 2000), 2000, 685–688.

[24] Kay, S.
Fundamentals of Statistical Signal Processing. Estimation Theory.
Englewood Cliffs, NJ: Prentice-Hall, 1993.

Paulo A. C. Marques (S'97—M'04) received the B.S. degree in electronics and telecommunications engineering from Instituto Superior de Engenharia de Lisboa (ISEL) in 1990 and the E.E., M.Sc., and Ph.D. degrees in electrical and computer engineering from Instituto Superior Técnico (IST) in 1993, 1997, and 2004, respectively.

He is a professor at ISEL, Department of Electronics and Communications Engineering. He is also a researcher with the Communication Theory and Pattern Recognition group at Institute of Telecommunications. His research interests are remote sensing, signal processing, image processing, and communications.

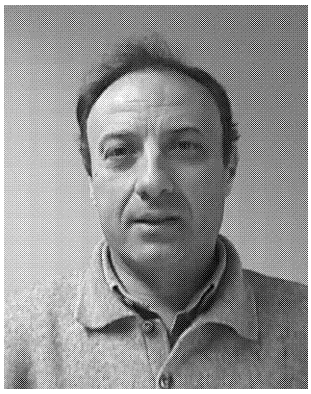

José M. Bioucas Dias (S'87—M'95) received the E.E., M.Sc., and Ph.D. degrees in electrical and computer engineering, all from Instituto Superior Técnico (IST), Technical University of Lisbon, Portugal, in 1985, 1991, and 1995, respectively.

He is currently an assistant professor with the Department of Electrical and Computer Engineering of IST. He is also a researcher with the Communication Theory and Pattern Recognition Group of the Institute of Telecommunications. His research interests include remote sensing, signal and image processing, pattern recognition, and communications.